Helmholtz-Zentrum Dresden-Rossendorf (HZDR)

HZDR
HELMHOLTZ ZENTRUM
DRESDEN ROSSENDORF

High Dielectric Transparent Film Tailored by Acceptor and Donor Codoping

Huang, D.; Shi, Y.; Younas, M.; Khan, R. T. A.; Nadeem, M.; Shati, K.; Harfouche, M.; Kentsch, U.; Liu, Z.; Li, Y.; Zhou, S.; Kuznestov, A.; Ling, F. C.-C.;

Originally published:

October 2022

Small 18(2022), 2107168

DOI: https://doi.org/10.1002/smll.202107168

Perma-Link to Publication Repository of HZDR:

https://www.hzdr.de/publications/Publ-35303

Release of the secondary publication
on the basis of the German Copyright Law § 38 Section 4.

High dielectric transparent film tailored by acceptor and donor co-doping

Dong Huang [1], Yingli Shi [1], Muhammad Younas [2], Rao Tahir Ali Khan [3], Muhammad Nadeem [2], Khaqan Shati [3], Messaoud Harfouche[4], Ulrich Kentsch[5], Shengqiang Zhou [5], Andrej Kuznestov [6], Francis Chi-Chung Ling *[1]

1 *Department of Physics, The University of Hong Kong, Hong Kong, 999077, P. R. China*

2 *Polymer Composite Group (PCG), Physics Division, PINSTECH, P. O. Nilore, Islamabad, Pakistan*

3 *Electronic and Magnetic Materials Group (EMMG), Physics Division, PINSTECH, P. O. Nilore, Islamabad, Pakistan*

4 *Synchrotron Light for Experimental Science and Applications in the Middle East (SESAME), Allan 19252, Jordan*

5 *Helmholtz-Zentrum Dresden-Rossendorf, Institute of Ion Beam Physics and Materials Research, Bautzner Landstrasse 400, 01328 Dresden, Germany*

6 *Department of Physics, University of Oslo, PO Box 1048 Blinders, 0316 Oslo, Norway*

Abstract

Designing new material properties is a great endeavor for industry and science. The dielectric properties are of particular current interest since materials with high dielectric constants are in demand for transistors, capacitors, etc. In this context, there is a modern trend to exploit defect engineering in oxide ceramics, delivering unprecedentedly high dielectric performance. On the other hand, demonstrations of similar high dielectric performance in more reliable crystalline films are rare. Herein, we report such breakthrough via functionalization of donor-acceptor dipoles by compositional tuning in (Ga, Cu) co-doped ZnO films. As a result, in samples with optimized composition, the dielectric constant reaches ~200 as measured at 1 kHz at room temperature (comparing with e.g. ~25 in HfO_2 known as the prime dielectric material) and the optical transmittance in the visible wavelength reaches 80 %. Moreover, by

analyzing massive impedance spectroscopy data, we have discriminated prominent relaxation mechanisms in correlation with the dipole properties in our samples, that enables a consistent explanation of the dielectric constant as a function of frequency. The atomistic nature of the dipoles was revealed by applying systematic x-ray spectroscopy analysis. Indeed, prominent peak shifts of the Cu2p3/2 signatures were correlated with the appearance of the $Ga_{Zn}^{\cdot} - Cu_{Zn}'$ dipole configurations in (Ga, Cu) co-doped ZnO films. Notably, we observed similar trends for the dielectric properties, while synthesizing our samples by different methods, specifically using pulsed laser deposition and ion implantation, indicating general character of the phenomena.

Introduction

Dielectric material with a high dielectric constant (k) and low dielectric loss throughout a wide frequency range is one of the key components for the device size scale-down in nanoelectronics [1], as well as in the flexible and stretchable electronics (FSE) [2]. For the new generation nanoscale Si-based CMOS with 1-2 nm SiO_2 gate thickness, the electron tunneling from the gate into the gate electrode is unacceptably large for the device operation [1]. Thus, SiO_2 has to be replaced by the new high-k materials, and the development of such materials with k ~ 100 -2000 will be one of the key enabling factors in next generation nano-electronics [1]. In its turn, thin film transistor (TFT) is the key component for FSE. There are many advantages of using high-k materials for TFTs, e.g. (i) increasing the capacitance which leads to high saturated drain-source current (I_{DS}) while reducing the operating voltage; and (ii) enhancing the field-effect mobility of the TFTs [2]. Additionally, for transparent TFTs, the high-k materials must exhibit excellent transmittance under visible light. Moreover, some dielectrics even exhibiting high-k may confront some problems, such as unfavorable bandgap offset, thermal instability, and incompatibility with the fabrication processes [3-5]. For example, antimony oxide single crystals (down to 1.8 nm thick) prepared by a substrate-buffer-controlled chemical vapor deposition strategy exhibited spectacular high k~100 [6]; however, the substrate-sensitive manufacturing method hinders its large-scale and practical application. In practice, HfO_2 (k = 25) gate dielectric was firstly and continually adopted in FET structures by Intel due to its advantages, such as thermal stability, kinetic stability, and good transparency, corresponding to an "equivalent oxide thickness" of 0.9 nm [7-9]. However, its relatively low dielectric constant may limit next generation applications.

A novel defect engineering approach to enhance the dielectric constant and maintain the low dielectric loss was proposed and demonstrated experimentally in ceramic oxides (for example rutile TiO_2 [10] and ZnO [11]). This approach involves the acceptor and donor co-doping of oxides. If only donors are introduced, hopping of electrons between donor levels lead to large dielectric constant, but dielectric loss is large [11]. Hu et al [10] proposed that the large dielectric constant was associated with the formation of electron-pinned defect dipoles which comprised of the donor and acceptor dopants. In response to the external electric field, electrons from the donors hop while the acceptor binds the electron locally within the defect complex, thus leading to the low dielectric loss. Huang et al [11] studied in detail the dielectric properties of the ceramic samples, the electronic structure and phonon structure around the dopants using x-ray photoelectron spectroscopy (XPS) and Raman spectroscopy respectively and theoretical simulation. The results offered concrete evidence that the large dielectric constant was associated with the correlated barrier hopping between nearby defect complexes comprising of intrinsic defect and the dopants.

k-enhancement with this co-doping methodology has been widely studied in many other ceramic oxide systems with different dopants (for example, [10] [11] [12-14]). However, this methodology has not been successfully applied to polycrystalline thin films, which are of technology relevance to the TFTs. ZnO is a wide band gap semiconductor transparent in optical wavelength, which is widely used for transparent TFT application. Ga, as group-III element, is a well-recognized donor dopant for ZnO [15]. Copper Cu is possible candidate for acceptor doping [15], whereas the p-type conductivity was confirmed by Hall and Seeback measurements [16].

In the present work, transparent Cu-Ga co-doped ZnO films were fabricated by pulsed laser deposition (PLD). High-k enhancement was observed by optimizing the relative Cu-Ga doping composition. Frequency dependent dielectric properties and relaxation mechanisms were studied in detail. Two processes were identified, namely the correlated barrier hopping (CBH) and small polaron tunneling (SPT). Simulation study was performed using a micro-polarization model helping to understand the origin of the high-k nature. X-ray photoelectron spectroscopy (XPS) and X-ray absorption spectroscopy (XAS) studies were performed to study the electronic structures around the dopants revealing the formation of the defect dipoles. Very importantly, we unveiled that similar high-k tailoring trends can be realized by both the high-throughput large-area and area selective fabrication methods (PLD and ion implantation, respectively), fulfilling the criteria for practical applications.

Experimental procedure

ZnO-based films were fabricated on c-plane sapphire substrates via PLD from ceramic targets having different concentrations of Ga and Cu dopants. During the deposition process, the chamber's base pressure was controlled at 5×10^{-4} Pa. The substrates' temperature was set at 600 °C. All films were deposited at the oxygen partial pressures of 5 Pa. The KrF excimer laser (wavelength: 248 nm, pulse energy: 300 mJ, frequency: 2 Hz) was applied to ablate the ceramic targets for creating plasma plume. As a result, (Ga, Cu) ZnO films, with a range of compositions were synthesized and the compositions have been confirmed by X-ray photoelectron spectroscopy. Cu-Ga co-doped ZnO films were fabricated with systematically varying the Cu and Ga doping ratios, wherein, films with Ga=0.5 wt% and Cu=8 wt% exhibits the highest dielectric constants among the studied Ga-Cu compositions. Notably, in this paper, for clarity, we will present the data for only one Cu and Ga co-doping composition made by

PLD – $Ga_{0.5}Cu_8Zn_{91.5}O$ – as it showed the maximum dielectric performance. For reference, the data for corresponding purely Cu and Ga doped ZnO thin films, $Cu_8Zn_{92}O$ and $Ga_{0.5}Zn_{99.5}O$ respectively, are shown as well. The deposition time was adjusted to compare samples with the same thickness, while varying the composition. Importantly, a set of additional samples was fabricated by a combination of the PLD and ion implantation. Specifically, $Cu_8Zn_{92}O$ PLD sample was implanted with 250 keV Ga^+ ions with 5 different doses: D1 = $1 \times 10^{14}\ cm^{-2}$, D2 = $5 \times 10^{14}\ cm^{-2}$, D3 = $1 \times 10^{15}\ cm^{-2}$, D4 = $5 \times 10^{15}\ cm^{-2}$, D5 = $1 \times 10^{16}\ cm^{-2}$, labeling these samples D1-D5 in the rest of the paper. Importantly, the implants were performed along 7° of the c-axis direction.

To enable the electrical measurements, the films were deposited on the bottom electrode. The bottom electrode was ZnO film doped with 1 wt% Ga, making it highly n-type conductive [17]. For the Ga-implanted films, an Al film deposited by thermal evaporation was used as the bottom electrode. Then, Al contacts were deposited via thermal evaporation and used as the top electrodes. A precision impedance analyzer (E4990A, Keysight Ltd., USA) was used to acquire the impedance spectroscopy data. The data analysis was performed in terms of the complex formalisms, for the permittivity ε^* ($\varepsilon^* = \varepsilon' - j\varepsilon''$) and for the modulus M^* ($M^* = M' - jM''$). Notably, the permittivity and the modulus are interrelated: $\varepsilon^* = (M^*)^{-1}$. Initially, the dielectric loss spectroscopy ($\varepsilon''\ vs\ f$) was measured at the frequency (f) range of 20-10^7 Hz at room temperature. Further, the spectroscopic data were collected as a function of temperature in the range of 160-370 K while keeping the sample in a cryostat. The sample was cooled down by cold sample holder connected to the liquid nitrogen tank and then heated electrically up to 370 K.

Structural characterization was performed by X-ray diffraction (XRD), Scanning Electron Microscopy (SEM) and X-ray Photoelectron Spectroscopy (XPS). In particular, XRD was performed using the Cu-Kα_1 radiation (Bruker D8 Advance) and was adopted to investigate the crystalline quality. The microstructure was examined by a Supra 55 (Carl Zeiss) scanning electron microscope (SEM) equipped with an energy dispersive spectrometer (EDS, X-MaxN). The transmittance measurements were conducted using a UV-Vis spectrophotometer (Lambda 750, PerkinElmer). The XPS was performed using a Thermo Theta Probe instrument with monochromatic Al Kα radiation (hν = 1486.6 eV) operated at 15 kV and 15 mA. High resolution spectra were collected at a step size of 0.05 eV for core/Auger peaks. An area of about 1 × 1 mm^2 was gently cleaned with a 1 kV Ar^+ ion beam delivering a current of 1 μA for 10 s. Notably, in order to make quantitative conclusion from the XPS data the C1s spectra were recorded as a calibration for the Cu2p signal, while investigating the corresponding shifts in $Cu_8Zn_{92}O$ and $Ga_{0.5}Cu_8Zn_{91.5}O$ films. For SIMS measurements, the IONTOF TOF-SIMS V spectrometer was used. The morphology of the films was tested using atomic force microscopy (AFM, Multimode V, Veeco) in tapping mode. Representative illustrations of the XRD, SEM, AFM, SIMS, and optical transmission measurements are included in the Supplementary Materials.

The X-ray Absorption Fine Structure (XAFS) technique, and specifically the X-ray absorption near edge structure (XANES) as well as the Extended X-ray Absorption Fine Structure (EXAFS) measurements, were used to collect element-specific local structure information around the host and dopant cations. Both XANES and EXAFS data were acquired at the XAFS/XRF beamline at the Synchrotron-light for Experimental Science and Applications in the Middle East (SESAME, storage ring running at 2.5 GeV), Allan, Jordan. Measurements were performed

at room temperature. Multiple-scanned spectra of each sample were recorded to get sufficiently high signal to noise ratio. XANES data analysis/processing such as normalization, merging *etc.* was performed by Athena program of Demeter software package by following the standard procedures. The structural parameters were derived using the Artemis software package to fit the EXAFS data to the best theoretical model calculated by FEFF6 program to extract the theoretical backscattering paths, amplitudes and phase shift of the fitting models. For simulating the data for each spectrum, a theoretical model was designed by adding shells around the central excited atom and least-square iterating the fitting parameters, namely the E_0, the radial distances (R) and the σ^2 (Å^2) termed as Debye–Waller factor (DWF). The coordination number (N) could be iterated too, but due to their strong correlation with σ^2 (Å^2), the coordination numbers were kept fixed at the preset values generally known from the symmetry. Concerning the amplitude reduction factor (S_O^2), it was found from a "standard" (data from a sample with a well-known structure) and applied to a set of unknowns as a scaling factor.

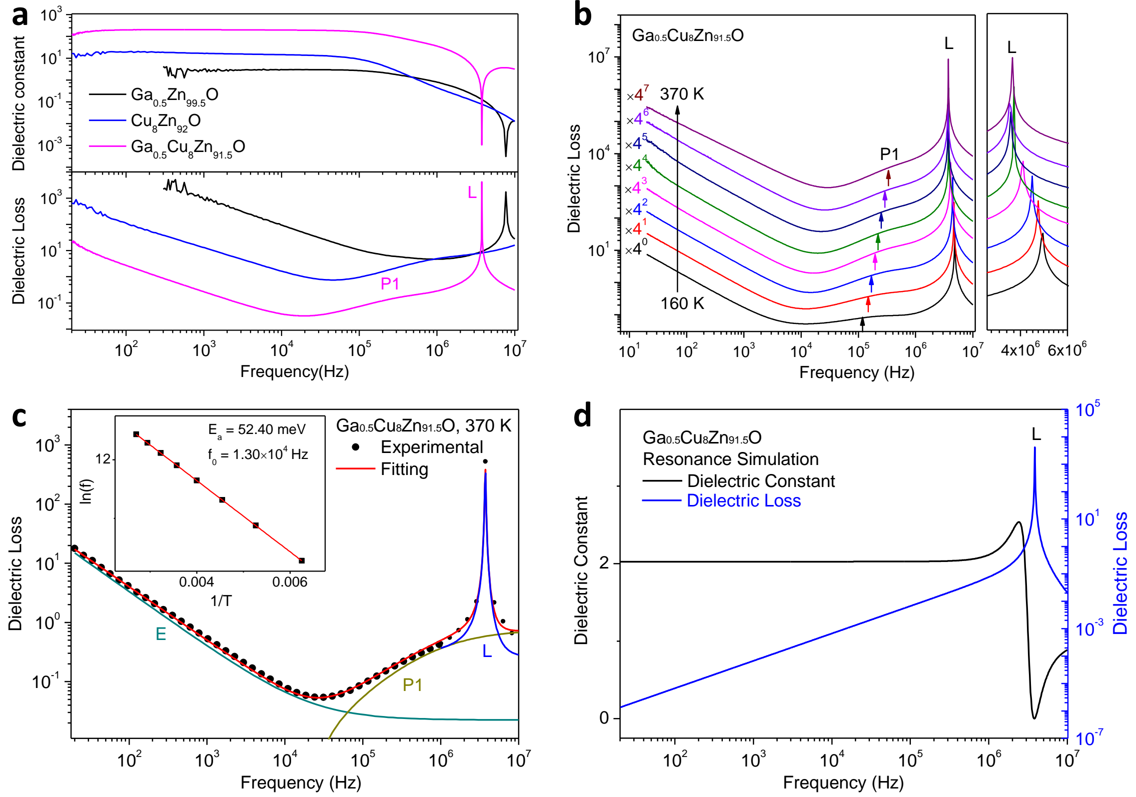

Fig. 1 Dielectric properties as a function of frequency. a Room temperature measurement of three samples: $Ga_{0.5}Cu_{99.5}ZnO$, $Cu_8Zn_{92}O$ and $Ga_{0.5}Cu_8Zn_{91.5}O$. **b** The dielectric loss as a function of frequency for $Ga_{0.5}Cu_8Zn_{91.5}O$ as measured at different temperatures with the interval of 30 K and the enlarged portion of the spectra corresponding to L part. **c** The simulation for the dielectric loss at 370 K in $Ga_{0.5}Cu_8Zn_{91.5}O$. The fitting components include the P1 component, the electrode (E) component and the Lorentizan resonance (L) component. The inset shows the Arrhenius plot of P1 for the temperature range studied. **d** Calculated L component at 280 K, as derived via the harmonic oscillator model.

The dielectric properties measured at room temperature in the frequency range from 20 to 10^7 Hz of $Ga_{0.5}Zn_{99.5}O$, $Cu_8Zn_{92}O$ and $Ga_{0.5}Cu_8Zn_{91.5}O$ films are presented in Fig. 1a. At 1 kHz, the dielectric constant/loss for the singly doped $Cu_8Zn_{92}O$ and $Ga_{0.5}Zn_{99.5}O$ films are 16/12 and 4/920, respectively. The high dielectric loss in $Ga_{0.5}Zn_{99.5}O$ is probably due to the delocalized free electrons provided by the Ga shallow donors [18]. For the Ga-Cu co-doped $Ga_{0.5}Cu_8Zn_{91.5}O$ film, the dielectric constant is 204 at 1 kHz and is well above ~100 for a wide frequency range from 20 to 10^5 Hz. The dielectric loss is relatively low (~0.27) at 1 kHz and still remains below 0.35 even at higher frequency of 1 MHz. Thus, the dielectric constant

enhancement in the $Ga_{0.5}Cu_8Zn_{91.5}O$ film can be attributed to the simultaneous incorporation of Ga donor and Cu acceptor. Due to the compensation process, relevant donor-like and acceptor-like defects, such as $Ga_{Zn}^{\cdot}$ and Cu_{Zn}', may potentially form defect complexes which are polarizable if applying external electric field, i.e. acting as "dipoles". In this way, for the $Ga_{0.5}Cu_8Zn_{91.5}O$ film, its dielectric constant increases to 204 and the loss still remains low ~0.27 as referred to 1 kHz. As for the dielectric loss, a relaxation peak in the range of 10^4-10^6 Hz (P1) and an additional sharp Lorentzian peak in the range from 10^6-10^7 Hz (L) are observed in Fig. 1(a).

Temperature dependent (160-370 K) dielectric loss vs frequency spectra of the $Ga_{0.5}Cu_8Zn_{91.5}O$ film are shown in Fig. 1b. As seen from Fig. 1b, the P1 relaxation peak shifts to higher frequencies with increasing temperature, which is typical in thermal activation process. In accordance with the Debye model, the dielectric constant is given as [19]:

$$\varepsilon^*(\omega) = \varepsilon_\infty + (\varepsilon_s - \varepsilon_\infty)/[1 + (j\omega t)^{1-\alpha}] \quad (1)$$

where j is the plural unit, ε_s and ε_∞ are respectively the permittivity at static and the light frequency, ω is the angular frequency, $\omega = 2\pi f$, t is the mean relaxation time. α is an empirical constant between 0 and 1 indicating the dispersion of the relaxation time, whereas $\alpha = 0$ refers to the classic Debye model having a constant relaxation time.

Notably, the sharp Lorentzian peak L is observed in the dielectric loss spectra in the frequency range of 10^6-10^7 Hz for both $Ga_{0.5}Zn_{99.5}O$ and $Ga_{0.5}Cu_8Zn_{91.5}O$ samples (Fig. 1(a)). The peak position of L does not follow the typical trend as of the thermal relaxation process (i.e. high frequency shift with decreasing temperature in Fig. 1b). In addition, its Lorentzian shape is also different from the broad dispersive peak observed in the thermal relaxation process. A

similar Lorentzian peak in the dielectric loss spectrum was also observed in $Sr_3Co_2Fe_{24}O_{41}$ sample and it was associated with an electronic harmonic oscillator model [20]. In the oscillation process, the resonance frequency decreases as the temperature increases and its corresponding dielectric response is dominated by the resonance behavior rather than the relaxation behavior [19, 20]. The frequency-dependent dielectric constant associated with the harmonic oscillation model is given by:

$$\varepsilon^*(\omega) = 1 + \frac{\omega_p^2}{(\omega_0^2 - \omega^2) + j\omega\gamma} \tag{2}$$

ω_p is the plasma frequency of the material, ω_0 is the characteristic resonance frequency of the oscillator in the absence of damping, and γ is the ratio of the damping coefficient to the inertia mass of the oscillator. Thus, considering the dielectric loss contribution from the relaxation and the oscillator and also the background contribution, the equation for the frequency-dependent dielectric loss becomes:

$$\tan\delta = \delta_0 + a_0\omega^{\alpha_0} + a_1\frac{(\omega t)^{1-\alpha_1}\cos\left(\frac{\alpha_1\pi}{2}\right)}{1+(\omega t)^{1-\alpha_1}\sin\left(\frac{\alpha_1\pi}{2}\right)} + \frac{\omega_p^2\omega\gamma}{\left(\omega_0^2-\omega^2\right)^2+\omega^2\gamma^2+\omega_p^2\left(\omega_0^2-\omega^2\right)} \tag{3}$$

where δ_0 is a constant, a_0 and a_1 are the correction coefficients. The detailed deduction process is presented in the Supplementary Material (section IV). The frequency-dependent dielectric loss data measured at different temperatures were fitted by Eq. (3). Fig. 1c shows a typical fitted curve to the data measured at 370 K, containing the relaxation component P1, the electrode component E, the oscillation component L, as well and their corresponding resultant superposition. As seen from Fig. 1c, the experimental spectrum is well described by the resultant fitted curve. The fitted parameters of δ_0, a_0, α_0, a_1, α_1, t, ω_p, ω_0 and γ

obtained from the iterating procedures at different temperatures are shown in supplementary (see Table S2 in Supplementary materials).

In Table S2, the relaxation time t for P1 decreases with increasing temperature and the relaxation frequency of P1 shifts to higher position correspondingly, implying a higher freeze-out probability at lower temperature. The activation energy of the thermal relaxation process was found to be 52.40 meV by the Arrhenius plot fitting (see the inset in Fig. 1c).

To characterize the dielectric response mechanism of the oscillation process, the damping ratio ζ is defined as the ratio of the damping coefficient in the oscillation system to the critical damping coefficient (without damping), i.e. $\zeta = \gamma/(2\omega_0)$. For $\zeta = 0$, only resonance-type dielectric response occurs without damping force. While ζ increases, the dielectric response would transfer from the resonance-dominated ($\zeta < 1$) to the relaxation-dominated ($\zeta > 1$) and the dielectric loss will broaden accordingly. Calculated from the fitted γ and ω_0 values tabulated in Table S2, ζ increases with increasing temperature from 0.020 at 160 K to 0.041 at 370 K. These low values of ζ (< 1) indicates the resonance-dominated nature of the peak. It would be interesting to study the contribution of the harmonic oscillator to the dielectric constant and loss. Dielectric constant and loss at different frequencies were calculated by the harmonic oscillator model (eqs S6-S8) with the fitted parameters ω_p, ω_0 and γ at the temperature of 280 K (see Fig. 1d). The modelled and experimental Lorentzian dielectric loss peaks coincide at ~3-4 MHz. The modelled dielectric constant is smaller than 3 throughout the whole frequency range, indicating that the oscillator process cannot contribute to the experimentally observed high permittivity.

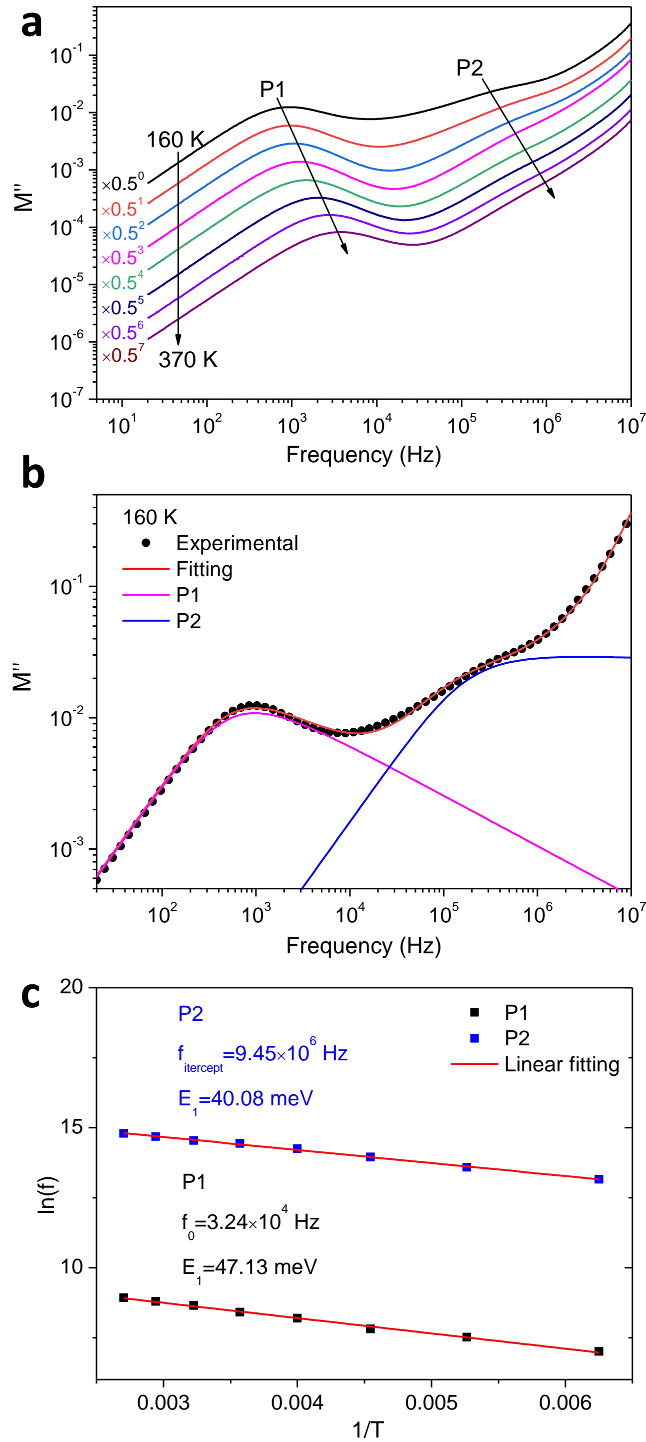

Fig. 2 Data and analysis of the imaginary part of the electric modulus (M'') in $Ga_{0.5}Cu_8Zn_{91.5}O$ film at different temperatures as a function of frequency. a Data in the range of 160-370 K (interval of 30 K). Each spectrum is presented with exponential factor of 0.5 as the temperature increases. **b** The simulation and fittings to the data measured at 160 K. The fitting component includes the P1 relaxation and P2 relaxation. Note that background term $M_e w^e$ has not been presented. **c** The Arrhenius plot for P1 and P2.

The complex electric modulus $M^* = M' - jM''$ is defined as the inverse of the complex permittivity ε^* and is typically used to explore the dielectric relaxation with a broad distribution of relaxation times [21]. To further explore the relaxation behavior, the frequency-dependent spectra of the imaginary part of electric modulus (M'' vs f) were taken at different temperatures (shown in Fig.2(a)). Two broad peaks are observed, namely in the frequency ranges of 10^3-10^4 Hz and 10^5-10^6 Hz. The one at 10^3-10^4 Hz will be demonstrated in the upcoming paragraph having the similar characteristic frequency as P1, and the other one is labbled as P2. Both peaks shift to high frequencies with increasing temperature.

To simulate the data the general formula of electric modulus M^* was used: [21]

$$M^*(\omega) = M_\infty\left(1 - \int_0^\infty \frac{\rho(\tau)}{1+j\omega\tau} d\tau\right) \tag{4}$$

where $M_\infty = 1/\varepsilon_\infty$ is the high-frequency limit of M^*, and $\rho(\tau)$ is the distribution function of the relaxation time τ. For ZnO, $\rho(\tau)$ follows the empirical Cole-Davidson (CD) distribution [22]:

$$\rho_{CD} = \begin{matrix} \frac{sin(\pi\beta)}{\pi\tau}\left[\frac{\tau}{\tau_{CD}-\tau}\right]^\beta, & \text{for } \tau < \tau_{CD} \\ 0, & \text{for } \tau > \tau_{CD} \end{matrix} \tag{5}$$

where $0 < \beta < 1$, $\int_0^\infty \rho_{CD}(\tau)d\tau = 1$ and τ_{CD} is the temperature dependent characteristic relaxation time. $M''(\omega)$ is thus shown to be:

$$M''(\omega) = M_\infty(cos\theta)^\beta \sin(\beta\theta) \tag{6}$$

where $\theta = \arctan(\omega\tau_{CD})$. Adding the background term $M_e w^e$, Eq. (6) containing multiple relaxation processes becomes:

$$M''(\omega) = M_e \omega^e + \sum_{i=1}^{2} M_i [\cos(\arctan(\omega\tau_i))]^{\beta_i} \sin[\beta_i \arctan(\omega\tau_i)] \quad (7)$$

where M_i and M_e are equivalent to $1/\varepsilon_i$ and $1/\varepsilon_e$ indicating the light-frequency limit of M^*, $\alpha_0$is the exponent, β_i is the range from 0 to 1 indicating the dispersion of relaxation time, τ_i is the characteristic relaxation time.

The M'' vs f data taken at each of the temperatures were fitted by Eq. 7. One of the typical results (data at 160 K) is shown in Fig. 2b, which contains the contributions from P1, P2 and their resultant superposition in good agreement with the experimental data. The fitted parameters M_e, e, M_1, τ_1, β_1, M_2, τ_2 and β_2 for different temperatures are tabulated in Table S3 (see Supplementary Materials-V).

As shown in Table S3, the relaxation times τ_1 and τ_2 decrease while their relaxation frequencies ($1/\tau$) increases with increasing temperature. Arrhenius fitting on the log f vs 1/T yielded good fitting; and the fitted activation energies were 47.13 meV and 40.08 meV for P1 and P2, respectively (see Fig. 2c). For P1, its characteristic frequency is $3.24 \times 10^4\ Hz$, close to that of the relaxation identified in Fig. 1c ($1.30 \times 10^4\ Hz$), indicating these two relaxations are likely identical. Concerning the P2 relaxation, it will be shown and discuss later that it is not only simply thermally activation but rather related to electron tunneling process.

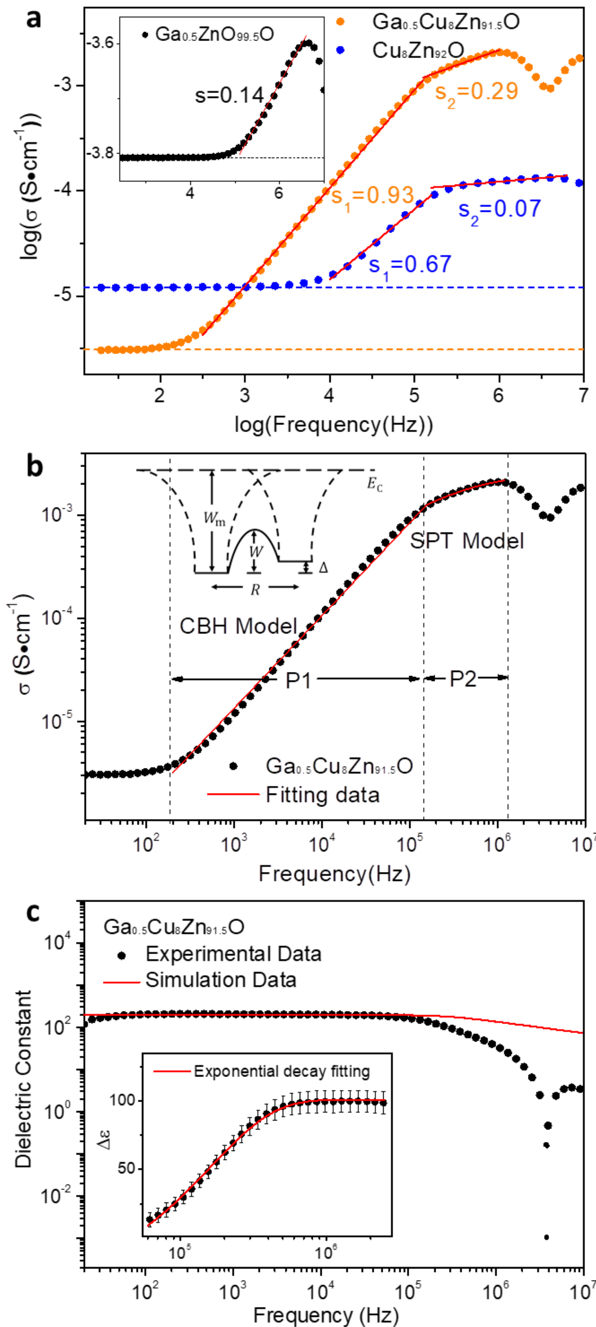

Fig. 3 The total conductivity and the dielectric constant simulation in terms of the Correlated Barrier Hopping (CBH) model and Small Polaron Tunneling (SPT) model. a The total conductivity vs frequency at room temperature for $Cu_8Zn_{92}O$ and $Ga_{0.5}Cu_8Zn_{91.5}O$, as well as the data for $Ga_{0.5}Zn_{99.5}O$ shown in the inset. **b** The total conductivity vs frequency data fitting for $Ga_{0.5}Cu_8Zn_{91.5}O$ using CBH in the range of 200-10^5 Hz and SPT models in the range of 10^5-10^6 Hz. The inset represents a schematic of the band diagram correlating with the processes in the CBH and SPT models. **c** Fitting of frequency-dependent dielectric constant data measured in $Ga_{0.5}Cu_8Zn_{91.5}O$. In the inset, the dots represent the deviation $\Delta\varepsilon$ between the simulation value and the experimental data, and the line is the fitting curve of $\Delta\varepsilon\ vs\ f$ under the assumption that the effective dipole concentrations exponentially decay with increasing frequency; demonstrating excellent accuracy of the analysis.

Frequency dependent ac conductivity of the Ga-doped, Cu-doped and Ga-Cu co-doped ZnO samples was measured to reveal the relaxation mechanisms, for which their data were shown in Fig 3a ($Ga_{0.5}Cu_8Zn_{91.5}O$ and $Cu_8Zn_{92}O$ samples) and its insert ($Ga_{0.5}Zn_{99.5}O$). The ac conductivity is given by the universal dielectric response law [23]:

$$\sigma(f) = \sigma_{dc} + \sigma_0 f^s, \qquad (8)$$

where σ_{dc} is the dc conductivity, σ_0 is a constant, f is the frequency of the driving electrical field, and $0 < s < 1$ is the frequency exponent and. In the log-log plot like Fig. 3a, the ac conductivity decreases linearly with the frequency in a certain frequency range and saturates at σ_{dc} at low frequency with $\sigma_{dc} \gg \sigma_0 f^s$. σ_{dc} and $\sigma_0 f^s$ are dependent on the band conduction and relaxation, respectively. σ_{dc} depends on the electron concentration and mobility, and thus it is sensitive to donors and compensating defects. For instance, in the $Ga_{0.5}Zn_{99.5}O$ film, σ_{dc} exhibits the maximum absolute value (logσ_{dc}=-3.8) because of electrons introduced by the donor dopant Ga and the absence of Cu acceptor. $\sigma_0 f^s$ term is associated to the relaxation processes involving the motions of electrons and ions, hopping and tunneling between equilibrium sites [24]. In a wide frequency range from 10 to 10^7 Hz, different relaxation processes dominate in different frequency ranges and result in the different values of s [24]. As shown in Fig. 3a, the linear fitting of the $Cu_8Zn_{92}O$ and $Ga_{0.5}Zn_{99.5}O$ data resulted in different s values in different frequency ranges. For $Ga_{0.5}Cu_8Zn_{91.5}O$ film with high k-value, linear fitting with Eq. (8) yields two s-values, namely 0.93 and 0.29 in the frequency ranges of 10^2~10^5 Hz and 10^5~10^6 Hz, respectively. It is known that s>0.90 is characteristic for the correlated barrier hopping (CBH) process and s<0.7 is characteristic for the small polaron tunneling (SPT) mechanism [24]. Therefore, the present result implies that

in the high-k $Ga_{0.5}Cu_8Zn_{91.5}O$, the CBH process and SPT process dominate in the frequency ranges of 10^2-10^5 Hz and 10^5-10^6 Hz, respectively. As shown in Fig. 2, the electrical modulus study revealed two relaxation processes P1 and P2, which dominated at frequencies range lower than 10^5 Hz and above 10^5 Hz, respectively. Thus, it is plausible to correlate the processes P1 and P2 to the CBH and the SPT processes, respectively.

In the CBH model, electrons are thermally activated to hop over the correlated potential barrier between two neighboring sites with a separation R (as shown in the insert in Fig. 3b). Assuming the electronic configuration exhibits the energy level W_m at the E_C - W_m, where E_C is the conduction band minimum. Δ is the asymmetric energy difference induced in two neighboring configurations due to the applied electric field. Furthermore, columbic potentials of two adjacent sites would overlap and then result in lowering the barrier from W_m to W, promoting the electron hopping. Assuming that at least one electron occupies the configurations, the electron would hop over the barrier between these two equilibrium sites with thermal activation [25-27]. It is given:

$$W = W_m - \frac{e^2}{\pi\varepsilon\varepsilon_0 R} \quad (9)$$

$$s = 1 - \frac{6k_BT}{W_m - k_BT\ln(1/f\tau_0)} \quad (10)$$

where τ_0 is the relaxation time, k_B is the Boltzmann constant.

A polaron would be formed if an electron trapped at a defects site causing the local lattice distortion results in lowering of total energy (inclusive of electronic and distortion), and the electron is trapped in the potential well resulted from the carrier-induced atomic displacement. Assuming that the polarons are localized and not overlapping [28], electron

hopping from the localized polaron state to the neighboring vacant defect site is unlikely but tunneling may happen. Therefore, the frequency exponent of s correlated with the SPT is limited by the probability of tunneling, being lower than that for the CBH. For SPT it is given [27, 29],

$$s = 1 - \frac{4}{ln(1/(f\tau_0)) - W_H/(k_B T)} \quad (11)$$

$$f = f_0 \exp(-2kR) \exp(-\frac{W_H}{k_B T}) \quad (12)$$

where τ_0 is the characteristic relaxation time, equal to $1/f_0$, k_B is the Boltzmann constant, W_H is the effective tunneling barrier, R is tunneling distance and k $(k = 2\pi/\lambda)$ is the localized electron wave vector.

The ac conductivity spectrum of $Ga_{0.5}Cu_8Zn_{91.5}O$ was well fitted by the CBH and SPT models in the frequency ranges from 200 Hz to 10^5 Hz and from 10^5 Hz to 10^6 Hz, respectively (Figure 3b), and the corresponding fitting parameters are tabulated in Table S4 (see Supplementary Material-V). For the CBH model fitting, the fitting values of W_m and τ_0 for P1 are 1.35 eV and 3.52×10^{-5} s. In the CBH model, the relaxation process is involved with an electron hopping between two nearby equilibrium sites of energy level E_C-W_m with a separation R, which would led to a dipole moment μ=eR [24]. The effective hopping distance R between the two neighboring sites could be calculated by Eq. (9), yielding 0.55 nm. For the SPT model, the best fit of W_H is 43.4 meV, consistently with the values deduced from the Arrhenius fitting in the inset in Fig. 2b. Notably, from Table S4, $\tau_0 = 1/f_0 = 3.47 \times 10^{-12}\ s$. In the SPT model, the localized electron could transport to the neighboring site via tunneling, leading to a dipole. From the Eq. (12) and the P2 Arrhenius plot fitting in the inset in Fig. 2b, the intercept $f_{intercept}$ could be defined as

$$f_{intercept} = f_0 \exp(-2kR) \qquad (13)$$

where $k = 2\pi/\lambda$ is the localized electron wave vector. Substituting the values of $f_{intercept}$ and f_0 into the Eq. (13), the ratio of the tunneling distance to electron's wavelength (R/λ) is 0.82. It would be interesting to estimate the tunneling distance *R*, if the approximate value of λ can be known. In analogy to the infinite potential well model, the highly localized electron's wavelength is equal to two times the lattice constant. Given that for the ZnO wurzite structure having the lattice constants of a=b=0.323 nm and c=0.516 nm, λ is approximated as in the range of 0.64-1.03 nm. Therefore, the tunneling distance could be estimated to be $R \sim 0.52 - 0.84$ nm. All-in-all, the electrons hopping or tunneling between two neighboring sites acting as a dipole under external electrical field explains the large dielectric constant in the $Ga_{0.5}Cu_8Zn_{91.5}O$ sample over a wide frequency range.

To simulate the static dielectric constant, Lorentz, Onsager and Kirkwood consecutively proposed different models to correlate the dielectric matrix and external electric field. Eq. (S13) (see Supplementary Material-VI) shows that the static dielectric constant is restricted to the dipoles concentration when the hopping and tunneling distance is calculated and the dipole moment μ is known. The dipole's concentration is restricted to these electrons and equilibrium sites. Accounting that Cu atoms are far more abundant comparing to Ga atoms, we may assume that the Ga content restricts the effective dipole concentration (N_v) in $Ga_{0.5}Cu_8Zn_{91.5}O$. More specifically, in the fits, the N_v for P1 and P2 were best fitted with $N_v = 9.35 \times 10^{18}\ cm^{-3}$ and $N_v = 6.18 \times 10^{19}\ cm^{-3}$, respectively, as shown in Fig. 3c. Note that Ga concentration was nearly $1 \times 10^{20}\ cm^{-3}$, implying that only a portion of the Ga-dopant is engaged into the dipoles. The critical limiting parameter may be the separation between the neighboring defects or complexes; meaning that for separations above the critical value, the

electron hopping or tunneling cannot occur. Further, based on Eq. (S13), the ε_s static dielectric constant for P1 and P2 are estimated to be 21.49 and 193.45, respectively. To estimate the dielectric frequency dependence, Debye assume the relaxation times for all the dipoles are identical. However, practically, due to the local distortion and electronic statues differences, the overall relaxation time would display a broad distribution function $\rho(\tau)$, rather than an identical value. The frequency-dependent dielectric constant from 20 Hz to 10^7 Hz could be computed via the integration on the relaxation time distribution of Cole-Davidson via Eq. (S15), as presented in Fig. 3c. As shown in Fig. 3c, the fitting curve coincides well with the experimental data exhibiting good frequency stability in the frequency range below 10^5 Hz. At the low frequency range, lower than 10^2 Hz, a minor deviation may be due to the electrode polarization. At 1 kHz, the calculated experimental dielectric constant is 199 which is in excellent agreement with the experimental value of 204. However, the fitting curve significantly deviates from the experimental data for the frequencies higher than 10^5 Hz. To explore the deviation, the fitting versus experimental data difference ($\Delta\varepsilon$) is plotted as a function of frequency in the inset of Fig. 3c. Importantly, the trend is well fitted by the exponential decay factor of $\exp(-\frac{f}{f_D})$, where $f_D = 1.62 \times 10^5\ Hz$. As shown in Fig. 3b, SPT is the dominant relaxation process at high frequencies >10^5 Hz. Theoretically, the tunneling distance is frequency dependent ($R = \frac{1}{2k}[ln\left(\frac{1}{w\tau_0}\right) - \frac{W_H}{k_BT}]$) [24] , decreasing from 0.90 nm to 0.52 nm at nearly 10^5 Hz, which is approaching the limitation of R value-lattice constant (c=0.52 nm), as shown in Fig. S6. Thus, the probability of the electron transition to neighboring defect site would exponentially decrease as the tunneling distance decrease with the frequency increasing. Further, the defect dipole cannot form in this case and the dipole concertation would also exponentially decrease, resulting in the deviation from the

simulation. To sum up, the enhanced dielectric performance is associated with P1 and P2 relaxations in correlation with the CBH and SPT mechanisms.

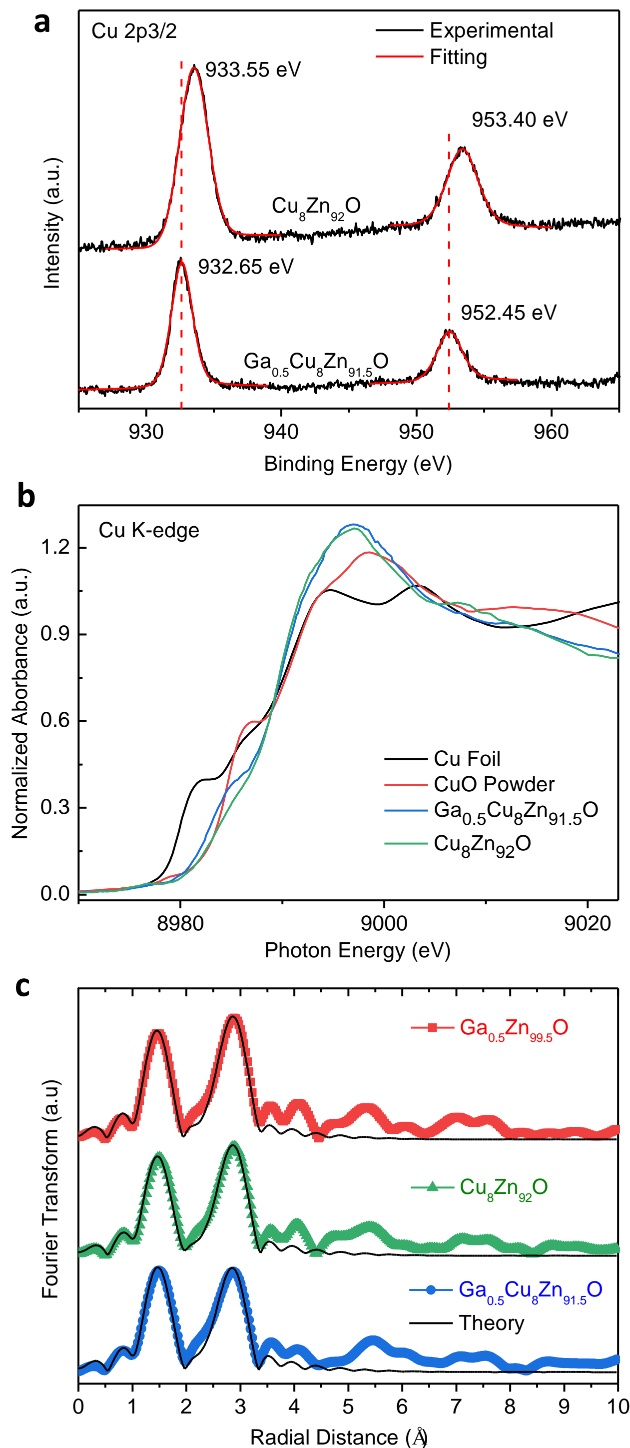

Fig.4 Examples of the X-ray analysis. a XPS data showing the Cu 2p spectra for the $Cu_8Zn_{92}O$ and $Ga_{0.5}Cu_8Zn_{91.5}O$ films. **b** The XANES spectra at the Cu K-edge of $Cu_8Zn_{92}O$ and $Ga_{0.5}Cu_8Zn_{91.5}O$ samples including reference samples, e.g. Cu foil and CuO powder. **c** Magnitude of the Fourier transform of the EXAFS spectra at the Zn K-edge of $Ga_{0.5}Zn_{99.5}O$, $Cu_8Zn_{92}O$ and $Ga_{0.5}Cu_8Zn_{91.5}O$ samples compared with theoretical model (black lines).

XPS and XAS studies were performed to characterize the local electronic and structural changes caused by the dopants. Fig. 4a shows the Cu2p spectra for the $Cu_8Zn_{92}O$ and $Ga_{0.5}Cu_8Zn_{91.5}O$ films. In $Ga_{0.5}Cu_8Zn_{91.5}O$, two peaks located at 932.65 eV and 952.45 eV correspond to the 2p3/2 and 2p1/2 electrons of Cu in Cu(I)-O bond indicating that the Cu dopants are acceptors as expected [30]. However, in the $Cu_8Zn_{92}O$ film, the 2p3/2 and 2p1/2 signals locate at 933.55 eV and 953.40 eV, implying there is a shift as compared to the corresponding signatures in $Ga_{0.5}Cu_8Zn_{91.5}O$. In the Cu(II)-O bond, the corresponding signals of 2p core levels mainly locate at about 933~935 eV and 953~955 eV [31]. In accordance with literature, for Cu(II), the main 2p core level's signal is accompanied with satellite peaks at ~ 9 eV higher than the binding energies [31]. In $Cu_8Zn_{92}O$, no satellite peaks are found indicating that Cu exists as Cu(I). Thus, the binding energy shift in Fig. 4a cannot be attributed to the Cu valence state differences. Importantly, all peaks were calibrated to the standard carbon signatures (see in Fig. S7 in Supplementary Materials-VII), confirming that the shift in Fig. 4(a) are not attributed to the instrumental artifact either. Therefore, we conclude that it is Ga doping that induces the binding energy shifts for Cu-positions in Fig. 4a. In $OCuZn_3$ tetrahedron of $Cu_8Zn_{92}O$, Cu^+ ion and another three Zn^{2+} ions sit at the tetrahedral vertex and bond with the central oxygen. Accounting for the electronegativity of Cu^+ (1.90) and Zn^{2+} (1.65), the central oxygen atom prefers to bond with Cu^+ ion in the bond structure of Cu^+-O-Zn^{2+} leading to high asymmetry in the relative oxygen position. In $OCuGaZn_2$ tetrahedron of $Ga_{0.5}Cu_8Zn_{91.5}O$, $Ga_{Zn}^{\cdot}$ and Cu_{Zn}' may engage into a dipole configuration $Ga_{Zn}^{\cdot} - Cu_{Zn}'$. Importantly, the electronegativity of Ga^{3+} ions (1.81) is higher than that of Zn^{2+} ions (1.65), nearly approaching that of Cu^+ ions (1.90). So that, the spatial asymmetry of oxygen in Cu^+-O-Zn^{2+} would be lowered as Ga^{3+} ion substitutes the Zn^{2+} forming the Cu^+-O-Ga^{3+} configuration.

Thus, the longer Cu-O bond length in the $Ga_{0.5}Cu_8Zn_{91.5}O$ film leads to lower binding energy as compared to that in the $Cu_8Zn_{92}O$ sample, as seen in Fig. 4a.

To explore the co-doping effect more precisely, the XANES and EXAFS measurements were applied to analyze the local structural change around the metal ions. Fig. 4b compares the XANES spectra at the Cu K-edge of $Cu_8Zn_{92}O$ and $Ga_{0.5}Cu_8Zn_{91.5}O$ samples including reference samples, specifically Cu foil and CuO powder. A clear change is observed in the Cu K-edge XANES features resulting in the shift of ~0.7eV while comparing $Ga_{0.5}Cu_8Zn_{91.5}O$ and $Cu_8Zn_{92}O$ samples. Correlating with the XPS data. The observed XANES features of $Ga_{0.5}Cu_8Zn_{91.5}O$ and $Cu_8Zn_{92}O$ samples are different from that of Cu foil showing absence of Cu metal clustering in these samples. It should be noted that the Cu K-edge XANES features of the samples do not match with that of CuO standard manifesting that Cu is not present in a separate CuO phase in these samples either [32, 33].

Moreover, the signature of $Ga_{Zn}^{\cdot} - Cu_{Zn}'$ is revealed by the Zn K-edge, specifically using EXAFS to investigate the microscopic arrangements around the cations, which may contain either undistorted or orientationally disordered ZnO_4 tetrahedral. Indeed, Fourier transforms (both experimental data and fits) of the Zn K-edge spectra of all the samples are shown in Fig. 4c and the best-fitted parameters are listed in Table S5 (see Supplementary Material-VIII). For the Zn K-edge, the fits were performed in R-space in the 1–3.5 Å range. The single scattering involving the oxygen atoms of the 1st shell, the zinc atoms of the 2nd shell and oxygen atoms of the 3rd shell were included in the fitting procedure. The peak at 1.5 Å is ascribed to the first shell of oxygen atoms related to the position of the Zn–O bonding distance, and the second peak contains contribution of Zn–Zn (second shell) and Zn–O (third shell). Noticeable and systematic changes were observed and shown in Table S5 in Supplementary Materials-VIII. In

particular, there is a prominent increase in Zn-Cu radial distances in $Ga_{0.5}Cu_8Zn_{91.5}O$. The increased 2nd shell Zn-Cu radial distances with reduced DWF in the $Ga_{0.5}Cu_8Zn_{91.5}O$ sample, i.e., when Cu atoms replace Zn atoms, suggests the presence of Ga in close proximity of Cu in the formation of Ga-Cu complexes, i.e. $Ga_{Zn}^{\cdot} - Cu_{Zn}'$ consistently with the rest of the data in Figs.1-4..

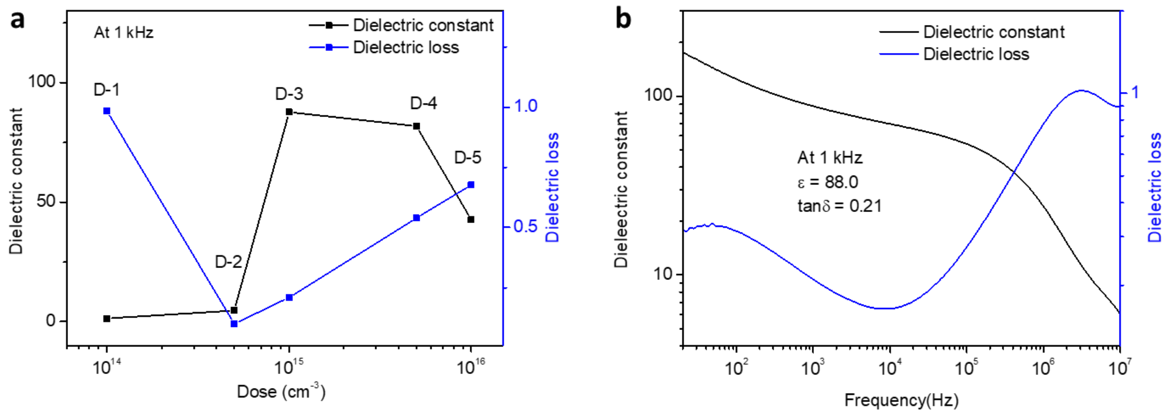

Fig. 5 Dielectric analysis of Ga implanted $Cu_8Zn_{92}O$. a The dielectric constant and loss at 1 kHz of $Cu_8Zn_{92}O$ implanted with different doses of Ga ions, D1 = $1 \times 10^{14}\ cm^{-2}$, D2 = $5 \times 10^{14}\ cm^{-2}$, D3 = $1 \times 10^{15}\ cm^{-2}$, D4 = $5 \times 10^{15}\ cm^{-2}$, D5 = $1 \times 10^{16}\ cm^{-2}$. **b** The dielectric constant and loss vs frequency spectra of D-3.

In order to prove the general character of the observed phenomena, we have tested alternative fabrication methods, in particular by implanting Ga into $Cu_8Zn_{92}O$ film to check the dielectric constant variation trends. Different doses of Ga were implanted into $Cu_8Zn_{92}O$ to realize the acceptor-donor defect complex similar to that in $Ga_{0.5}Cu_8Zn_{91.5}O$ PLD sample highlighted in Figs. 1-4. Fig. 5 shows the dielectric properties of such Ga implanted $Cu_8Zn_{92}O$ thin films. Comparing the 1 kHz data for all implanted samples in Fig. 5a, the optimal dielectric properties were observed in sample D3, i.e. implanted with Ga of $1 \times 10^{15}\ cm^{-2}$, in particular featuring the dielectric constant of 88 and the loss of 0.21, respectively. Moreover, the frequency-dependent measurements of D3 (see Fig. 5b) shows that the dielectric constant remains relatively high in a wide range of frequencies. The trend of degrading properties in D4 and D5 is probably due to generation of bigger number of radiations induced defects while in D1 and D2 the Ga concentration was likely insufficient. Indeed, the SIMS measurement confirmed ~$10^{20}\ cm^{-3}$ at the maximum of the Ga depth profile in D3 (see Fig. S4b in Supplementary Materials-III) [34]. According to the AFM images of $Cu_8Zn_{92}O$ (see Fig. S5 in Supplementary Materials-III) before and after the implantation, the surface roughness has

not raised significantly, indicating that the implants did not deteriorate the surface morphology. Thus, we observed similar k-enhancements in the PLD grown Cu-Ga co-doped ZnO films and in the films co-doped by ion implantation, implying that this high-k dielectric tailoring could be realized by both the high-throughput large-area and area selective fabrication methods. Note that, ion implantation is a well-developed technology for forming micro- and nano-structures for semiconductor chips.

Conclusion

In this study, a new approach to optimize the dielectric properties by acceptor-donor co-doping has been demonstrated in (Ga_x, Cu_y) $Zn_{1-x-y}O$ films fabricated with pulse laser deposition (PLD) or, alternatively, exchanging the co-doping step by the ion implantation. In either case, the structural and chemical analysis revealed no secondary phases or inhomogeneity's with the accuracy of the measurements. Importantly, for the fully PLD processed films, upon testing a range of concentrations, the optimal composition of $Ga_{0.5}Cu_8Zn_{91.5}O$ has resulted into the dielectric constant and dielectric loss of 204 and 0.27, respectively, as measured at 1kHz at room temperature. Moreover, by analyzing the impedance spectroscopy data, we have discriminated two prominent relaxation mechanisms in $Ga_{0.5}Cu_8Zn_{91.5}O$ labelled P1 and P2. The in-depth ac conductivity analysis suggested two mechanism to explains these relaxations: the correlated barrier hopping and small polaron tunneling. Considering options for the dipole polarization for P1 and P2 as well as accounting for the Cole-Davidson relaxation time distribution and the static dielectric constant speculated from the Kirkwood's polarization theory, we simulated the frequency-dependent dielectric constant obtaining consistent fits with the experimental data. The atomistic nature of these dipoles was confirmed by applying systematic x-ray spectroscopy analysis. Spectacularly, prominent peak shifts of the Cu2p3/2 signatures were correlated with the local chemical environment of Cu_{Zn} in $Ga_{0.5}Cu_8Zn_{91.5}O$, specifically indicating the existence of the $Ga_{Zn}^{\cdot} - Cu_{Zn}'$ dipole configurations. The corresponding increase in the 2nd shell radial distances of the Zn K-edge in the $Ga_{0.5}Cu_8Zn_{91.5}O$ sample was consistent to the hypothesis of Zn atoms being replaced by Cu atoms while adding Ga; thus, positioning Ga in a close proximity of Cu in the form of $Ga_{Zn}^{\cdot} - Cu_{Zn}'$ dipole. Notably, similar evolution of the dielectric

properties was observed in samples synthesized by ion implantation potentially enhancing the industrial applicability of the high dielectric constant (Ga_x, Cu_y) $Zn_{1-x-y}O$ films.

Acknowledgement

The study is supported by the Key-Area Research and Development Program of Guangdong Province (No.2020B010170002), the Guangdong Natural Science Fund (No. 2019A1515012164). The research is also under the Norway-China collaboration, which is enabled by the INTPART Program at the Research Council of Norway (grant nr 261574).

References (notes: the references would be updated automatically by endnote in each modification. And the originally imported reference styles may differ from each other. So, all the references will be manually formatted at last.)

1. Auciello, O., et al., *Super high-dielectric-constant oxide films for next-generation nanoelectronics and supercapacitors for energy storage.* MRS Bulletin, 2020. **45**(3): p. 231-238.
2. Wang, B., et al., *High- k Gate Dielectrics for Emerging Flexible and Stretchable Electronics.* Chem Rev, 2018. **118**(11): p. 5690-5754.
3. Robertson, J., *High dielectric constant gate oxides for metal oxide Si transistors.* Reports on Progress in Physics, 2006. **69**(2): p. 327-396.
4. Fortunato, E., P. Barquinha, and R. Martins, *Oxide semiconductor thin-film transistors: a review of recent advances.* Adv Mater, 2012. **24**(22): p. 2945-86.
5. Yim, K., et al., *Novel high-κ dielectrics for next-generation electronic devices screened by automated ab initio calculations.* NPG Asia Materials, 2015. **7**(6): p. e190-e190.
6. Yang, K., et al., *Ultrathin high-kappa antimony oxide single crystals.* Nat Commun, 2020. **11**(1): p. 2502.
7. S. Natarajan, e.a., *A 14nm logic technology featuring 2nd-generation FinFET interconnects, self-aligned double patterning and a 0.0588 µm2 SRAM cell size.*, in *In Proc. 2014 IEEE International Electron Devices Meeting 3.7.1–3.7.3*. **2014**.
8. Li, W., et al., *Uniform and ultrathin high-κ gate dielectrics for two-dimensional electronic devices.* Nature Electronics, 2019. **2**(12): p. 563-571.
9. Choi, J.H., Y. Mao, and J.P. Chang, *Development of hafnium based high-k materials—A review.* Materials Science and Engineering: R: Reports, 2011. **72**(6): p. 97-136.
10. Hu, W., et al., *Electron-pinned defect-dipoles for high-performance colossal permittivity materials.* Nature Materials, 2013. **12**: p. 821-826.
11. Huang, D., et al., *Electron-pinned defect dipoles in (Li, Al) co-doped ZnO ceramics with colossal dielectric permittivity.* Journal of Materials Chemistry A, 2020. **8**(9): p. 4764-4774.
12. Cheng, X., Z. Li, and J. Wu, *Colossal permittivity in ceramics of TiO2 Co-doped with niobium and trivalent cation.* Journal of Materials Chemistry A, 2015. **3**(11): p. 5805-5810.
13. Bovtun, V., et al., *Wide range dielectric and infrared spectroscopy of (Nb+In) co-doped rutile ceramics.* Physical Review Materials, 2018. **2**(7).
14. Dong, W., et al., *Colossal permittivity with ultralow dielectric loss in In + Ta co-doped rutile TiO2.* Journal of Materials Chemistry A, 2017. **5**(11): p. 5436-5441.
15. Vines, L. and A. Kuznetsov, *Bulk Growth and Impurities.* Semiconductors and Semimetals, 2013: p. 67-104.
16. Suja, M., et al., *Realization of Cu-Doped p-Type ZnO Thin Films by Molecular Beam Epitaxy.* ACS Appl Mater Interfaces, 2015. **7**(16): p. 8894-9.
17. Pak, C.M., et al., *Post-growth annealing study of heavily Ga-doped zinc oxide grown by radio frequency magnetron sputtering.* Journal of Physics D: Applied Physics, 2013. **46**(13).
18. McCluskey, M.D. and S.J. Jokela, *Defects in ZnO.* Journal of Applied Physics, 2009. **106**(7): p. 071101.

19. Jonscher, A.K., *Dielectric relaxation in solids*. 1983, London: Chelsea Dielecctrics Press. 380.
20. Tang, R., et al., *Dielectric relaxation, resonance and scaling behaviors in Sr3Co2Fe24O41 hexaferrite.* Sci Rep, 2015. **5**: p. 13645.
21. Pathmanathan, K. and J.R. Stevens, *Improved analysis of ionic-conductivity relaxation using the electric modulus with a cole-davidson distribution.* Journal of Applied Physics, 1990. **68**(10): p. 5128-5132.
22. Zhao, X., et al., *Role of defects in determining the electrical properties of ZnO ceramics.* Journal of Applied Physics, 2014. **116**(1): p. 014103.
23. Jonscher, A.K., *The 'universal' dielectric response.* Nature, 1977. **267**(5613): p. 673-679.
24. Elliott, S.R., *A.c. conduction in amorphous chalcogenide and pnictide semiconductors.* Advances in Physics, 1987. **36**(2): p. 135-217.
25. Pike, G.E., *ac Conductivity of Scandium Oxide and a New Hopping Model for Conductivity.* Physical Review B, 1972. **6**(4): p. 1572-1580.
26. Elliott, S.R., *A theory of a.c. conduction in chalcogenide glasses.* Philosophical Magazine, 1977. **36**(6): p. 1291-1304.
27. Long, A.R., *Frequency-dependent loss in amorphous semiconductors.* Advances in Physics, 1982. **31**(5): p. 553-637.
28. Emin David, H.T., *Studies of small-polaron motion IV. Adiabatic theory of the Hall effect.* Annals of Physics, 1969. **53**(3): p. 439-520.
29. Schnakenberg, J., *Polaronic Impurity Hopping Conduction.* Physica Satus Solidi (b), 1968. **28**(2): p. 623-633.
30. Lasse Vines, A.K., *Bulk Growth and Impurities.* Semiconductors and Semimetals, 2013: p. 67-104.
31. John F. Moulder , W.F.S., Peter E. Sobol, *Handbook of X-ray Photoelectron Spectroscopy: A Reference Book of Standard Spectra for Identification and Interpretation of XPS Data*, ed. J. Chastain. 1992: Physical Electronics Division, Perkin-Elmer Corporation. 261.
32. Tiwari, N., et al., *Structural and magnetic studies on (Fe, Cu) co-doped ZnO nanocrystals.* Journal of Physics and Chemistry of Solids, 2017. **104**: p. 198-206.
33. Tiwari, N., et al., *Local structure investigation of (Co, Cu) co-doped ZnO nanocrystals and its correlation with magnetic properties.* Journal of Physics and Chemistry of Solids, 2016. **90**: p. 100-113.
34. Morvan, E., et al., *Channeling implantations of Al+ into 6H silicon carbide.* Applied Physics Letters, 1999. **74**(26): p. 3990-3992.